fractal and fractional

Article

Seepage-Fractal Characteristics of Fractured Media Rock Materials Due to High-Velocity Non-Darcy Flow

Xiaoming Zhao [1,2], Binbin Yang [1,3,*], Yulong Niu [2,4] and Changde Yang [3]

1 School of Civil Engineering, Xuchang University, Xuchang 461000, China
2 College of Civil and Transportation Engineering, Hohai University, Nanjing 210098, China
3 School of Mines, China University of Mining and Technology, Xuzhou 221116, China
4 China Three Gorges Corporation, Wuhan 430010, China
* Correspondence: yangbinbin@cumt.edu.cn

Abstract: Under the influence of internal and external factors, a fracture network is easily generated in concrete and rock, which seriously endangers project safety. Fractal theory can be used to describe the formation and development of the fracture network and characterize its structure. Based on the flow balance in the node balance field, Forchheimer's law is introduced to derive the control equation of high-velocity non-Darcy flow in the fracture network. The fracture network is established according to the geological parameters of Sellafield, Cumbria, England. A total of 120 internal fracture networks are intercepted according to 10 dimensions (1 m, 2 m, . . . , 10 m) and 12 directions (0°, 30°, . . . , 330°). The fractal dimension, equivalent hydraulic conductivity (K), and equivalent non-Darcy coefficient (β) of the fracture network are calculated, and the influence of the fractal dimension on K and β is studied. The results indicate that the fractal dimension of the fracture network has a size effect; with the increase in the size, the fractal dimension of the fracture network undergoes three stages: rapid increase, slow increase, and stabilization. In the rapid increase stage, K and β do not exist. In the slow increase stage, K exists and is stable, and β does not exist. In the stabilization stage, K and β both exist and are stable. The principal axes of the fitted seepage ellipses of K and β are orthogonal, and the main influencing factors are the direction and continuity of the fracture.

Keywords: fractal dimension; fracture network; equivalent hydraulic conductivity; equivalent non-Darcy coefficient

check for updates

Citation: Zhao, X.; Yang, B.; Niu, Y.; Yang, C. Seepage-Fractal Characteristics of Fractured Media Rock Materials Due to High-Velocity Non-Darcy Flow. *Fractal Fract.* **2022**, *6*, 685. https://doi.org/10.3390/fractalfract6110685

Academic Editors: Shengwen Tang, Lei Wang and Wojciech Sumelka

Received: 16 October 2022
Accepted: 15 November 2022
Published: 18 November 2022

1. Introduction

The development of fractal theory provides an effective theory for the study of civil engineering materials such as concrete and rock mass. Concrete and rock are common fracture materials and are widely used in dams, tunnels, and mining projects. The development of an internal fracture in materials reduces the strength of the structure, which poses greater risks to the construction project and causes changes in internal water pressure, leading to various seepage problems and affecting the safety of the project. As a new theoretical method of describing the structural characteristics of a fracture network in fracture media, fractal theory has achieved considerable development in the field of engineering materials [1–3], providing a scientific theoretical basis for the study of complex fracture media such as concrete and rock mass [4–6]. Many engineering practices and experimental studies have shown that the trace length follows the power law distribution of the fractal dimension, which can be expressed by the fractal dimension [7]. The internal fractures crisscross to form a connected fracture network. The location, trace length, and direction of the fracture reflect the structure of the fracture network, giving it typical characteristics [7,8]. Fractal geometry provides a suitable mathematical framework for characterizing and simulating the geometric characteristics of many complex non-Eulerian shapes in nature and has proved to be suitable for fracture media such as concrete and rock mass [9,10].

In the current research, most scholars have focused on the fractal study of the fracture structure and strength characteristics of engineering materials such as concrete [11,12]. For the statistics on internal fractures, fracture network reconstruction, and seepage-fractal characteristics, there are few studies.

Fracture propagation not only reduces the strength of materials and causes fractures, breakage, overturning, and other engineering disasters, but also increases the seepage channel of water, changes the permeability of materials, and seriously affects the safety of dam projects. Many dam accidents worldwide are caused by the seepage of fractures [13,14], resulting in many casualties and property losses. In addition, traditional projects such as tunnels and mines involve seepage problems of the fracture media. The fracture network in rock mass provides seepage channels for high-pressure groundwater, which will cause serious water inrush accidents [15,16]. Injecting an active expansion agent into concrete, rock, and other fracture materials can play an effective role in plugging leakage, significantly reducing permeability, and improving project safety [17,18]. With the development of science and technology, people have attached importance to energy and environmental issues, and many new underground engineering technologies have emerged, such as geological storage of radioactive waste and pollutants [19], underground storage of CO_2 [20], and the development and utilization of geothermal and oil resources, which involve seepage of fractured rock masses. Therefore, it is important to study the seepage characteristics of fractured media to effectively ensure the long-term safe and stable operation of construction projects.

The fracture medium consists of a low permeability block and a high water conductivity fracture network. Compared with the high water conductivity of the fracture network, the permeability of the block in the entire medium can be ignored. It can be simply considered that in a fractured rock mass, seepage does not occur in the rock but flows along the fractures. The water inflow and outflow at the fracture nodes are the same, and the flow through the fracture network has reached a balance. Many scholars have carried out in-depth research on the seepage characteristics of fracture media to determine the relationship between the hydraulic conductivity of the fracture network and the fracture structure and obtain the seepage field of fracture media [21–23].

With the deepening of research, numerous tests have determined that, with the increase in the hydraulic gradient, the seepage characteristics of fractures no longer obey the linear Darcy's law, and there is a nonlinear relationship between velocity and hydraulic gradient. The larger the hydraulic gradient, the more obvious the phenomenon of deviation from Darcy law, that is, non-Darcy flow [24,25]. Visualization technology can intuitively display the behavior of fluid flow in the fracture intersection [26]. For the cross-fracture model, when the Reynolds number is large, the flow rate changes nonlinearly, the fluid begins to flow nonlinearly, and the pressure and flow rate no longer maintain a linear relationship [24,27]. Other experiments have shown that even if the flow velocity is very small, the fluid in the fracture network will also have obvious nonlinear flow [28]. The cubic law is generally used to calculate the seepage characteristics of each fracture in the discrete fracture network, and the constant hydraulic gradient is assumed. However, the cubic law often overestimates the seepage capacity of fluid through the fracture, which is different from the actual fluid flow [29–31]. Therefore, when calculating the seepage flow of each fracture, the applicable conditions of the cubic law should be fully considered, and an appropriate method should be selected to calculate the nonlinear flow of fluid in the fracture network.

The statistical parameters of a fracture affect the fractal characteristics and permeability of the fracture network at the same time. Fracture propagation in nature has a certain randomness, leading to the fractal dimension of the fracture network usually being non-integer [9]. Meanwhile, the permeability of the fracture network is affected by the fracture trace, aperture, direction, and density. With the increase in the trace length, aperture, and density, more fractures intersect with each other, changing the connectivity and leading to the change in the hydraulic conductivity of the fracture medium [32]. Some scholars have introduced correlation to calculate the permeability tensor and obtained the relationship between the fractal characteristics of the fracture network and the permeability of the equivalent fracture network according to the actual parameters [33]. The fractal expression of the fracture trace length can also be established through the correlation between the fracture aperture and trace length, and the variation law of equivalent permeability can be analyzed based on the numerical method; then, the tensor of hydraulic conductivity coefficient of the fracture network can be obtained [34]. Therefore, there is a certain relationship between the fractal characteristics and permeability of a fracture network. Exploring the seepage-fractal relationship of fracture media will further promote the application of fractal theory in engineering.

At present, the research in this field has mainly been focused on linear Darcy flow in the fault network and rarely involves high-velocity non-Darcy flow. The research on the equivalent hydraulic conductivity coefficient, equivalent non-Darcy coefficient, and their influencing factors is insufficient. Meanwhile, the relationship between the fractal dimension and K and B must also be further studied. In this study, a fracture network is established according to actual geological data. Then, a series of fracture networks with different sizes and angles are intercepted, and their fractal dimensions K and β are calculated. The influence of the fractal dimensions on K and β is explored, and the seepage-fractal characteristics of the fracture network are revealed.

2. Methodology

2.1. Fractal Dimension of Fractured Media

Fracture media such as concrete, rock mass, etc., exist widely in nature. When subjected to impact load or earthquake, fractures are generated in materials. With the increase in fractures, they connect with each other and form a fracture network. The fracture network of rock mass has typical self-similarity, which makes it possible to characterize the fracture network with the fractal dimension.

The fractal dimension of the fracture network can be calculated with Equation (1):

$$D(\psi) = \lim_{\delta \to 0^+} \frac{\log N(\delta)}{\log(1/\delta)} \tag{1}$$

where ψ is a bounded fracture network in two-dimensional Euclidean space, $N(\delta)$ is the number of elements forming a finite cover of the fracture, and δ is a bound on the length of the sets involved. Informally, δ is the size of each element used to cover the set, which is taken to approach 0. By changing the size of the element several times and calculating the number of elements covering the fracture, a series of data about $\delta - N(\delta)$ were obtained; then, the scatterplot of δ and $N(\delta)$ was made, the slope of the point set was calculated based on the least squares method, and the slope was the fractal dimension of the fracture network.

In this study, the box-counting method was used to calculate the fractal dimension of the fracture network. The image needed to be grayed to obtain a digital representation of the fracture network. In order to eliminate the background and all kinds of noise information, it was necessary to binarize the digital image and strengthen the image features of the fracture network. According to the image characteristics, the gray value of the pixel points on the fracture network image was set to 0 and 255, and the entire image showed a significant black-and-white effect. This allowed intuitive identification of fractures, and the fractal dimension of the fracture network was obtained, as shown in Figure 1. The fractal dimensions of the fracture network in Figure 1c,d were 1.646 and 1.651, respectively.

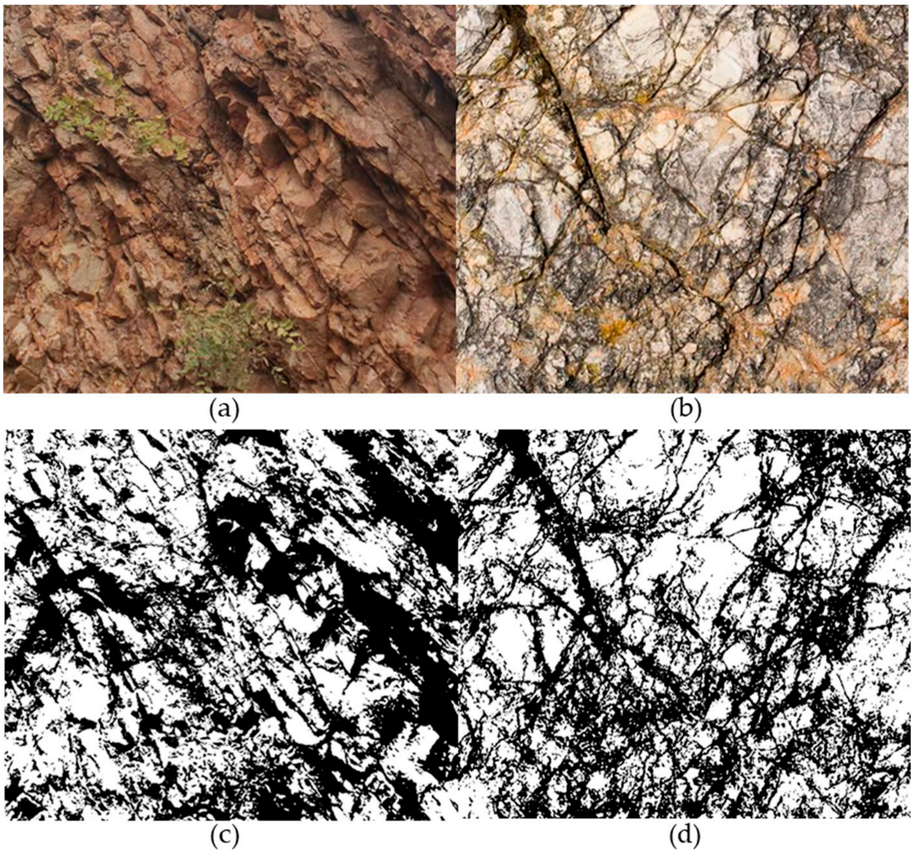

Figure 1. Graying and binarization of the fracture network. (**a**,**b**) The fracture network in Songshan Mountain, Dengfeng, Zhengzhou City; (**c**,**d**) grayscale and binary fracture network.

2.2. Discrete Fracture Network Generation

In this study, a new fracture network was generated based on the Monte Carlo method. The fracture network was affected by the statistical parameters of the fractures, in which the trace length and tendency were randomly generated, and the density and aperture were fixed.

The fracture network was composed of multiple fractures. When the fractures are generated, parameters such as the location, trace length, and direction of the fractures must be obtained. It was assumed that the fracture location followed a Poisson process, which can be realized by generating random numbers based on a recursive algorithm [7,34]. This algorithm ignores the integer part of the result and retains only the decimal part, as shown in Equation (2):

$$G_{i+1} = 27.0 \times G_i - INT(27.0 \times G_i) \quad (2)$$

where G_i is a random number of uniform distribution in the open interval (0,1), $INT()$ is the integer function, which returns the integer part of the real number inside ( ), and the initial value of G_0 can be obtained based on the multiplication congruential method. Taking a rectangular space in a Cartesian coordinate system to generate the fracture network, if the space coordinate satisfies $x \in [x_{s1},\ x_{s2}]$, $y \in [y_{s1},\ y_{s2}]$, the coordinates of the midpoint of each fracture can be obtained from the following equation [34]:

$$\begin{aligned} x_i &= G_i(x_{s2} - x_{s1}) + x_{s1} \\ y_i &= G_i(y_{s2} - y_{s1}) + y_{s1} \end{aligned} \quad (3)$$

In a fracture network, the trace length of a single fracture follows the power law distribution of the fractal dimension [34], as shown in Equation (4):

$$l = \frac{1}{\left(l_{\min}^{-D} + u(l_{\max}^{-D} - l_{\min}^{-D})\right)^{1/D}} \tag{4}$$

where l is the trace length, D is the fractal dimension, $l_{\max}$ and $l_{\min}$ are the maximum and minimum trace lengths in the fracture network, respectively, u is a random number subject to a uniform distribution in the closed interval [0,1].

The deviation degree between the direction of a single fracture and the main direction of fracture propagation usually follows the Fisher distribution [7]. If α is the angle of the fracture deviating from the average direction, it can be expressed as Equation (5):

$$\alpha = \cos^{-1}\left\{\frac{\ln[e^F - u(e^F - e^{-F})]}{F}\right\} \tag{5}$$

where F is the Fisher constant, which is mainly used to describe the deviation degree between the direction of a single fracture and the main direction of fracture propagation; the larger the F, the stronger the consistency of the overall propagation direction of the fracture. With Equations (4) and (5), we can obtain the trace length and propagation direction of fractures based on the Monte Carlo method. With Equations (2)–(5) and statistical data, all the data needed to generate the fracture network are obtained. In order to completely avoid the boundary effect, the gap width should be larger than half the maximum trace lengths [7]. Figure 2 shows the discrete fracture network generated under different fracture parameters, Table 1 shows the fracture parameters of Figure 2a, and Table 2 shows the fracture parameters of Figure 2b.

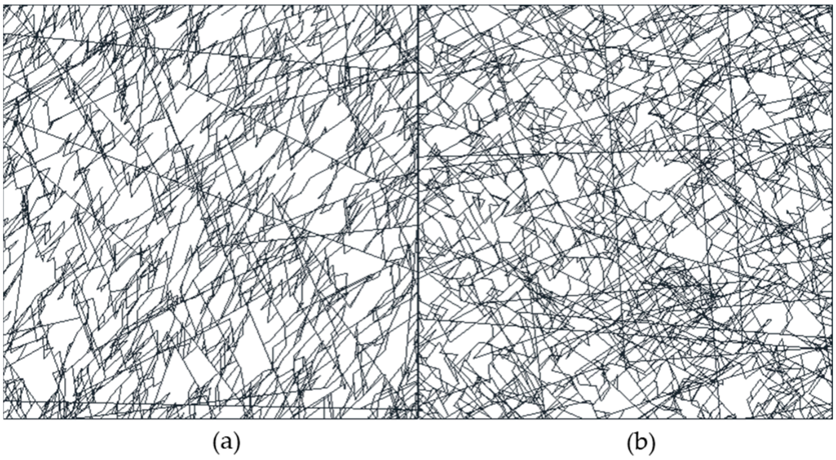

Figure 2. Discrete fracture network generated by different parameters. (**a**) Fracture parameters shown in Table 1; (**b**) fracture parameters shown in Table 2.

Table 1. Fracture network parameters of Figure 2a.

Fracture Group	Direction (°)		Trace Length (m)		Density (m^{-2})
	Mean	Standard Deviation	Mean	Standard Deviation	
1	148.7	2.6	12.8	2.1	1.1
2	142.5	2.9	10.6	1.6	1.8
3	71.6	2.1	14.5	2.2	4.3
4	28.1	2.6	13.8	2.4	4

Table 2. Fracture network parameters of Figure 2b.

Fracture Group	Direction (°)		Trace Length (m)		Density (m^{-2})
	Mean	Standard Deviation	Mean	Standard Deviation	
1	165.5	3.2	13.2	2	1.6
2	94.5	2.5	15.3	1.8	3.1
3	71.6	2.8	11.6	2.1	6.4
4	35.3	4.1	9.7	3.1	8.2

2.3. High-Velocity Non-Darcy Flow in a Fracture Network

It is generally considered that water is an incompressible fluid, and the amount of water flowing into and out of the fracture nodes is the same in a fracture network. When there are multiple fracture inflow or outflow nodes, the flow rate and direction of each fracture must be calculated separately. Based on the cubic law, the seepage model of fractured rock mass is constructed, the flow control equation is established, the boundary conditions and initial conditions are introduced, and the seepage law of water in the fracture network is solved.

In this study, in order to solve the high-velocity non-Darcy seepage field of a fractured rock mass and obtain the water head, flow rate, and velocity in the fracture, a seepage model of the fracture network was established, as shown in Figure 3. Each independent line in the area represents a fracture, reflecting the continuity condition of water flow at each fracture node, and the arithmetic sum of water inflow and outflow in each balance field was 0.

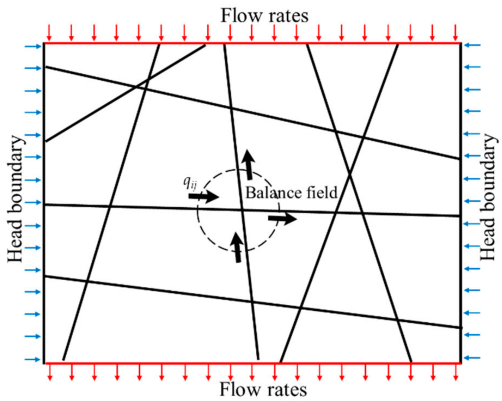

Figure 3. Schematic diagram of fracture balanced field and boundary conditions for flow analysis.

Suppose a fracture network is composed of N fracture nodes and M fractures, and fracture j corresponds to a segment with a fracture aperture b_j and line length l_j. Select a node i randomly in the fracture network, and there are N' fractures intersecting the ith node. According to the principle of flow conservation, the flow equation of the ith node can be expressed as Equation (6):

$$(\sum_{j=1}^{N'} q_j)_i + v_i = 0;\ (j = 1,\ 2,\ \cdots,\ N') \tag{6}$$

where q_j is the flow rate of fracture j into or out of node i, and v_i is the flow rate into or out of the fracture network at node i. When node i is located inside the fracture network, $v_i = 0$. Since there are N nodes in the fracture network, Equation (6) can be expressed in matrix form as follows:

$$AQ + V = 0 \tag{7}$$

where $V = (v_1,\ v_2,\ \cdots,\ v_N)^T$, $Q = (q_1, q_2, \cdots, q_M)^T$, and $A = \{a_{ij}\}_{N\times M}$ are the $N \times M$ order connection matrix of the fracture network, which describes the connection relationship between fractures and nodes in the fracture network. When fracture j does not connect with node i, $a_{ij} = 0$. When fracture j connects with node i and points to node i, $a_{ij} = +1$. When fracture j connects with node i and points away from node i, $a_{ij} = -1$. Then the head difference vector in the fault can be expressed as Equation (8):

$$\Delta H = A^T H \tag{8}$$

where $\Delta H = (\Delta H_1,\ \Delta H_2,\ \cdots,\ \Delta H_M)^T$ is the vector of order $M \times 1$, A^T is the transposition matrix of the connection matrix, and H is the node head vector of order $N \times 1$. The nodes in the fracture network belong to three categories. Category a: internal nodes where the total number is N_a. Category b: nodes with flux boundary conditions with a total number of N_b. Category c: nodes with head boundary conditions with a total number of N_c. The total number of nodes satisfy $N = N_a + N_b + N_c$. Considering the flow balance of nodes, Equation (7) can be further expressed as

$$\Delta H = {A_a}^T H_a + {A_b}^T H_b + {A_c}^T H_c \tag{9}$$

where $A_a^T,\ A_b^T,\ A_c^T$ are the transposed matrices of the connecting matrix of order $M \times N_a$, $M \times N_b$, and $M \times N_c$ respectively; $H_a,\ H_b,\ H_c$ are the water head vectors of order $N_a \times 1$, $N_b \times 1$, and $N_c \times 1$ respectively. Equation (7) can be rewritten as:

$$\begin{cases} A_a Q + V_a = 0 \\ A_b Q + V_b = 0 \\ A_c Q + V_c = 0 \end{cases} \tag{10}$$

where $V_a,\ V_b,\ V_c$ are the boundary flow rate vectors of order $N_a \times 1$, $N_b \times 1$, and $N_b \times 1$, respectively. Assuming that the fracture is simplified as a smooth parallel plate, according to the cubic law, the flow in the jth fracture can be expressed as the equation below owing to Darcy flow:

$$\begin{array}{l} q_j = k_f \cdot b_j d_j \cdot (\Delta H_j)/l_j = Tl_j \cdot (\Delta H_j) \\ Tl_j = \frac{\rho g b_j^3 d_j}{12\mu l_j} \end{array} \tag{11}$$

where k_f is the intrinsic permeability defined as $b^2/12$, ρ is the density of water, g is the acceleration of gravity, μ is the coefficient of viscosity, and b_j and d_j are the aperture and depth of the jth fracture element, respectively. In a two-dimensional seepage problem, $d_j = 1$. The matrix form of Equation (11) can be expressed as

$$Q = Tl \cdot (\Delta H) \tag{12}$$

where $Tl = diag(Tl_1,\ Tl_2,\ \cdots,\ Tl_M)$ take Equations (9) and (12) into Equation (10) to obtain the following equation:

$$\begin{array}{l} (A_a \cdot Tl \cdot A_a^T) H_a + (A_a \cdot Tl \cdot A_b^T) H_b + (A_a \cdot Tl \cdot A_c^T) H_c + V_a = 0 \\ (A_b \cdot Tl \cdot A_a^T) H_a + (A_b \cdot Tl \cdot A_b^T) H_b + (A_b \cdot Tl \cdot A_c^T) H_c + V_b = 0 \\ (A_c \cdot Tl \cdot A_a^T) H_a + (A_c \cdot Tl \cdot A_b^T) H_b + (A_c \cdot Tl \cdot A_c^T) H_c + V_c = 0 \end{array} \tag{13}$$

As shown in Figure 3, a constant head boundary is applied on the left and right sides of the fracture network, and a constant flow boundary is applied on the top and bottom. According to the boundary conditions, V_a, V_b, and H_c are known quantities, and H_a, H_b, and V_c are unknown quantities. The boundary flow rate V_c can be obtained by solving the following equation:

$$V_c = -\left(A_c \cdot Tl \cdot A_a^T\right) H_a - \left(A_c \cdot Tl \cdot A_b^T\right) H_b - \left(A_c \cdot Tl \cdot A_c^T\right) H_c. \tag{14}$$

However, in engineering, a high-velocity non-Darcy flow is more common in fractures. At this time, it is generally believed that it obeys Forchheimer's law [25,35,36]. The hydraulic gradient in the jth fracture can be expressed as

$$J_j = \frac{12\mu}{\rho g b_j^2} \frac{q_j}{b_j d_j} + \frac{\beta_j}{g} \left(\frac{q_j}{b_j d_j} \right)^2 = B_j q_j + C_j q_j^2 \quad (15)$$

where β_j is the non-Darcy coefficient, related to the aperture and roughness of the fracture. B_j and C_j are the coefficients that describe the energy losses of the flow caused by viscosity and inertia, respectively, and can be written as follows:

$$\begin{aligned} B_j &= \frac{12\mu}{\rho g b_j^3 d_j} \\ C_j &= \frac{\beta_j}{g b_j^2 d_j^2} \end{aligned} \quad (16)$$

We can calculate q_j and Tl_j by solving Equation (15).

$$q_j = \frac{-B_j + \sqrt{{B_j}^2 + 4C_j J_j}}{2C_j \cdot \Delta H_j} \cdot \Delta H_j = Tl_j \cdot (\Delta H_j), \quad (17)$$

$$Tl_j = \frac{-B_j + \sqrt{B_j^2 + 4C_j J_j}}{2C_j J_j} l_j. \quad (18)$$

A nonlinear equation group of the fracture network is formed by bringing Equation (18) into Equation (13); then, V_c can be solved by iterative method, as shown in Figure 4.

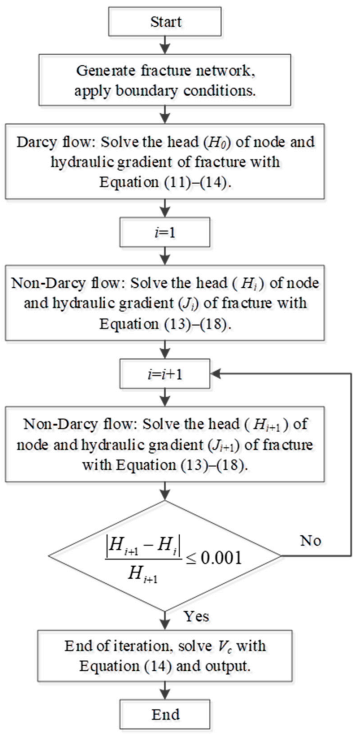

Figure 4. Flow chart for solving the non-Darcy flow of a fracture network.

2.4. *K* and *β* of a Fracture Network

As shown in Figure 3, assuming that the side length of the plane fracture network is L, and the flow rate on the upper and lower boundaries is 0, the hydraulic gradient acting on the fracture network owing to the Darcy flow can be expressed as:

$$J = \frac{1}{K} \cdot \frac{V_c}{L} \quad (19)$$

where K is the equivalent hydraulic conductivity reflecting the overall permeability of the fracture network. According to Forchheimer's law, the hydraulic gradient acting on the fracture network owing to the non-Darcy flow satisfies the following equation [35–37]:

$$J = \frac{1}{K}\frac{V_c}{L} + \frac{\beta}{g}\left(\frac{V_c}{L}\right)^2 \quad (20)$$

where β is the equivalent non-Darcy coefficient that describes the energy losses of the flow caused by inertia. By changing the hydraulic gradient and calculating the boundary flow rate, K and β can be obtained by fitting.

3. Case Study

3.1. Fracture Network for High-Velocity Non-Darcy Flow Calculation

British Nirex Co., Ltd. once conducted an engineering geological survey at a site in Sellafield, Cumbria, England, and obtained the occurrence and distribution characteristics of fractures in the region. The survey results have been used by many scholars to evaluate the equivalent hydraulic conductivity and the stress seepage coupling characteristics of the fractured rock mass.

In this study, the fracture network was generated by referring to the fracture parameters in the Sellafield area. The fracture parameter information is shown in Table 3. There were four groups of fractures, and the direction of the fractures followed the Fisher distribution. According to Equation (5), the angle deviating from the average direction can be calculated, and then the actual direction of each fracture can be obtained. According to the literature [7,34], the trace length of the fractures in the Sellafield area followed a power law distribution. The trace length was distributed between closed intervals [0.5, 250], and the fractal dimension of the trace length was 2.2. According to the fractal, more than 90% of the fracture traces were less than 2 m long. Based on the above conditions, the average trace length calculated by Equation (4) was 0.93 m.

Table 3. Fracture network parameters of Sellafield, Cumbria, England.

Fracture Group	Direction (°)	Fisher Coefficient	Fracture Width (μm)	Density (m^{-2})
1	21	10	65	4.6
2	87	10	65	4.6
3	145	5.9	65	4.6
4	148	9	65	4.6

In order to reduce the influence of the boundary effect, a fracture network was generated within a range of 300 m × 300 m. In this condition, $x \in [-150, 150]$, $y \in [-150, 150]$, and the midpoint coordinates of the fracture were calculated according to Equations (1) and (2). Since the average trace length of the fracture was 0.93 m, in the seepage-fractal study of the fracture network, a very small area met the requirements of the representative elementary volume and hydraulic conductivity tensor. In the 300 m × 300 m fracture network, the 15 m × 15 m range was selected as the research object, and it had the same center point. In the selected 15 m × 15 m fracture network, taking the midpoint of the analysis area as the benchmark, the square calculation areas with side lengths of 1 m, 2 m, . . . , 10 m were respectively intercepted for research. In order to further analyze whether the equivalent k and β formed a permeability ellipse under different fractal dimensions and side lengths, the analysis area was rotated counterclockwise from 0° to 330°, and the fracture network was intercepted at intervals of 30. A total of 12 fracture networks with the same size and different angles were obtained. Considering the influence of fractal, direction, and side length, a total of 120 different fracture networks were analyzed, as shown in Figure 5.

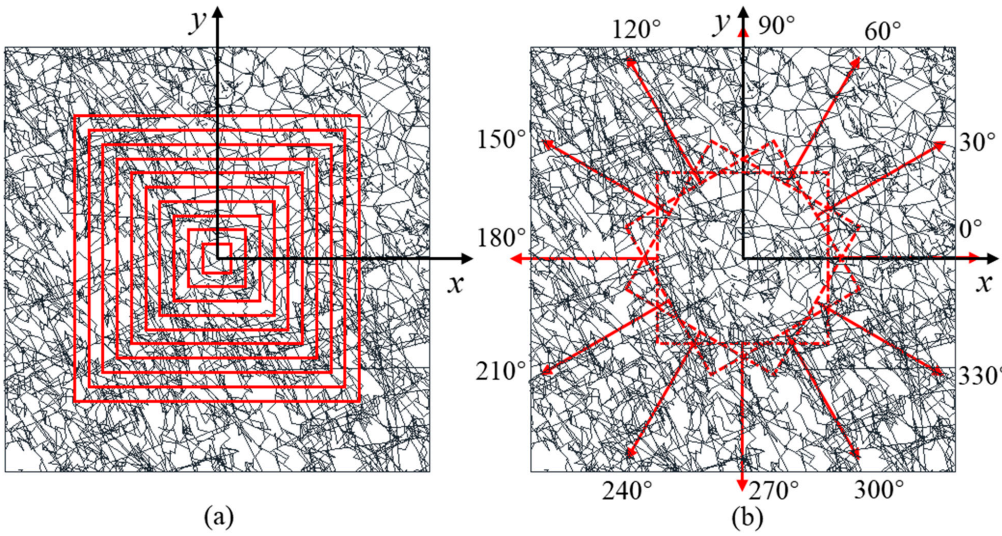

Figure 5. The 120 fracture networks with different side lengths and different directions. (**a**) Fracture networks with different side lengths of 1 m, 2 m, $\cdots$, 10 m; (**b**) fracture networks with different directions of 0°, 30°, $\cdots$, 330°.

3.2. Boundary Condition

Figure 6 shows the boundary conditions for high-velocity non-Darcy flow analysis. The upper and lower boundaries of the model were set as impermeable boundaries; the right boundary was set as the constant with a head equal to 0 m, the left boundary was also set as the constant head boundary, and the head value was the hydraulic gradient times the area side length. In order to obtain the equivalent k and β of the fracture network by fitting, the seepage conditions under five different hydraulic gradients were respectively set up for calculation and simulation; the hydraulic gradients were 10, 50, 100, 150, and 200, in turn.

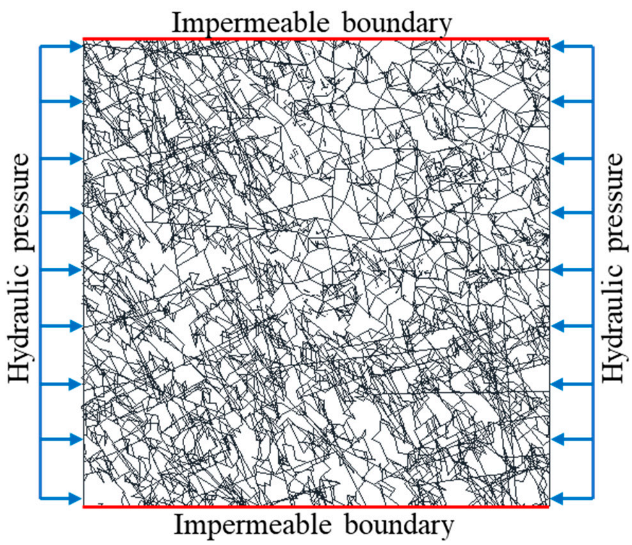

Figure 6. Boundary conditions for high-velocity non-Darcy flow analysis.

4. Results

4.1. The Existence of K with Different Fractal Dimensions

The fitting seepage ellipse of K with different fractal dimensions is shown in Figure 7. With the increase in fracture network size, the fractal dimension increases gradually. When $L < 4$ m, the fractal dimension increases rapidly, when $4 \le L \le 8$ m, the growth rate slows down, and when $L > 8$, it tends to be stable.

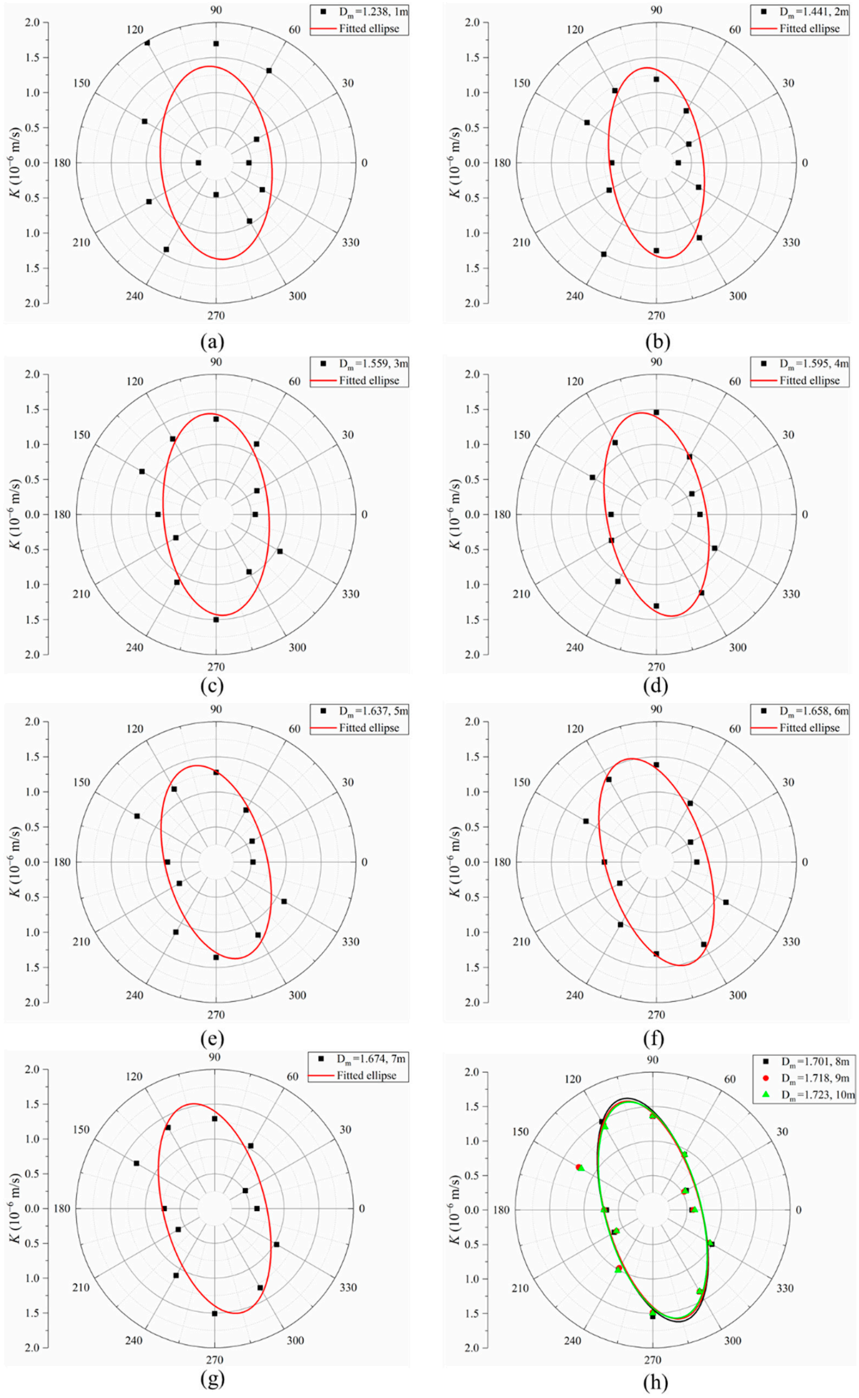

Figure 7. Fitting ellipse of K with different fractal dimensions towing to the high-velocity non-Darcy flow. (**a**) Fitting ellipse with D = 1.238, (**b**) fitting ellipse with D = 1.441, (**c**) fitting ellipse with D = 1.559, (**d**) fitting ellipse with D = 1.595, (**e**) fitting ellipse with D = 1.637, (**f**) fitting ellipse with D = 1.658, (**g**) fitting ellipse with D = 1.674, (**h**) fitting ellipse with D = 1.701, 1.718 and 1.723.

In Figure 7a, K has a minimum value in the direction of 180° and a maximum value in the 120° direction. The ratio of the maximum and minimum values is 7.79. In Figure 7b,c, the ratios of maximum and minimum values are 4.80 and 2.68, respectively. Obviously, with the rapid increase in the fractal dimension from 1.238 to 1.559, the calculated K is in an unstable state, significantly deviates from the seepage ellipse, and presents a certain randomness. At this time, K does not exist. In Figure 7d–h, as the fractal dimension gradually increases from 1.595 to 1.723 and tends to be stable at 1.723, the ratio of the maximum and minimum values of K does not change much, and they are all distributed in the closed interval [2.45, 2.96]. In this condition, K is in a stable state, approximately converges to the seepage ellipse, and K exists in the fracture network.

4.2. Variation in K with Different Fractal Dimensions of a Fracture Network

In Figure 7a, K obviously deviated from the fitted seepage ellipse in all directions, and its value is close to the ellipse in the 0°, 30°, 300°, and 330° directions. In other directions, it is far from the ellipse, especially in the 120° and 270° directions. The same phenomenon can be found in Figure 7b. In the 60°, 90°, 120°, and 270° directions, K almost coincides with the ellipse, while in the 150° and 240° directions, it is far from the ellipse. Compared with Figure 7a, with the propagation of the fracture network, K increases in some directions and decreases in others, showing a certain randomness.

In Figure 7c, K is distributed near the seepage ellipse, without obvious deviation, and the dispersion is significantly reduced. In the direction of the principal axis of the ellipse, K reaches the maximum. In Figure 7d–g, with the increase in fractal dimension, K does not change much in different directions, and the fitted seepage ellipse tends to be consistent. In Figure 7h, the fractal dimension and seepage ellipse change little. As the growth rate of the fractal dimension decreases, it is difficult to effectively improve the complexity of the fracture network. The non-Darcy flow in all directions tends to be stable, and K in all directions hardly changes. Obviously, with the increase in the fractal dimension, the dispersion of K gradually decreases, and finally converges to the seepage ellipse.

4.3. The Existence of β with Different Fractal Dimensions

Figure 8 shows the fitting seepage ellipse of β with different fractal dimensions. In Figure 8a,b, the calculated β seriously deviates from the seepage ellipse, which has no practical significance. In Figure 8c,d, a good seepage ellipse is formed, while β changes obviously in most directions. In Figure 8e–g, the length of the principal axis of the seepage ellipse of β has changed significantly. Obviously, with the increase in the fractal dimension from 1.238 to 1.674, the calculated β is in an unstable state, deviates from the seepage ellipse, and cannot represent the equivalent non-Darcy coefficient of the fractured rock mass. In Figure 8h, as the fractal dimension tends to be stable and approximately converges to 1.723, the calculated β tends to be stable and approximately converges to the seepage ellipse, which represents the equivalent non-Darcy coefficient of the fractured rock mass.

With the increase in the fractal dimension, the direction of the principal axis of the seepage ellipse does not change significantly. Compared with Figure 7, the principal axis of ellipse β is orthogonal to the principal axis of ellipse K. In the principal axis direction of ellipse β, β gets the maximum value, K is the minimum value, while in the principal axis direction of ellipse K, β gets the minimum value, and K is the maximum value.

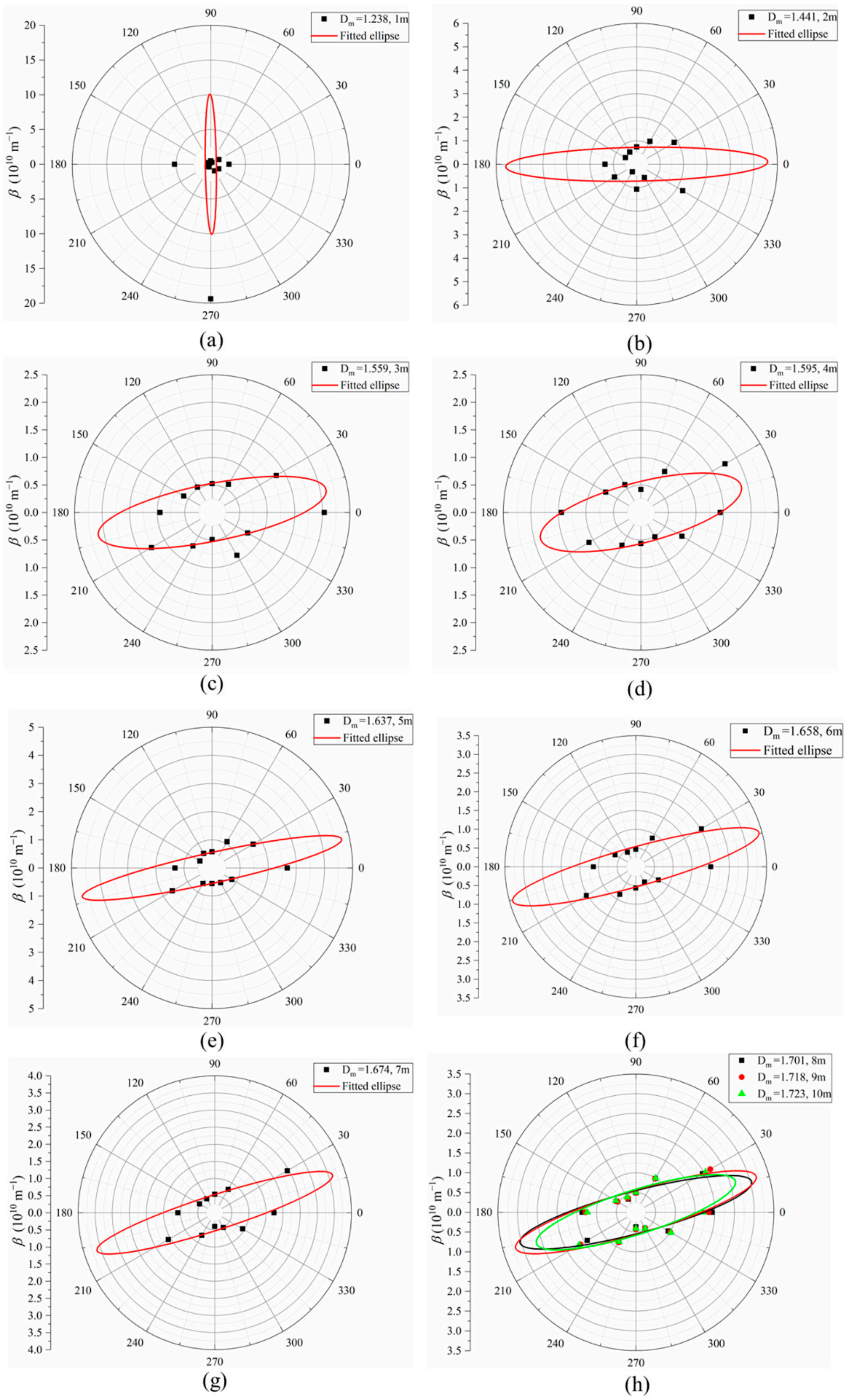

Figure 8. Fitting ellipse of β with different fractal dimensions owing to the high-velocity non-Darcy flow. (**a**) Fitting ellipse with D = 1.238, (**b**) fitting ellipse with D = 1.441, (**c**) fitting ellipse with D = 1.559, (**d**) fitting ellipse with D = 1.595, (**e**) fitting ellipse with D = 1.637, (**f**) fitting ellipse with D = 1.658, (**g**) fitting ellipse with D = 1.674, (**h**) fitting ellipse with D = 1.701, 1.718 and 1.723.

4.4. Variation in β with Different Fractal Dimensions of a Fracture Network

In Figure 8a, β has a maximum value in the 270° direction and a minimum value in the 120° direction. The ratio of maximum and minimum value of β is 99.79. In Figure 8b,c, the ratios of maximum and minimum values are 20.22 and 5.13, respectively. Obviously, as the fractal dimension increases rapidly from 1.238 to 1.559, the calculated β shows strong anisotropy and decreases rapidly.

In Figure 8d–h, with the decrease in the growth rate of the fractal dimension, the ratio changes little and is distributed in the closed interval [4.22, 6.12], indicating that the anisotropy of β tends to be stable.

4.5. Effect of Reynolds Number on K and β

When fluid flows in a single fracture, the Reynolds number (*Re*) can be expressed as

$$Re = \frac{\rho \overline{v} b}{\mu} = \frac{\rho q}{\mu d} \tag{21}$$

where, $\overline{v}$ and q are the average flow velocity and flow rate of the fluid in the fracture, respectively.

In Figure 9, when $Re < 1$, the hydraulic conductivity of a single fracture is almost unchanged, consistent with the theoretical results. When $Re > 1$, the hydraulic conductivity decreases rapidly with the increase in Re, which means that the flow rate and hydraulic gradient are no longer linear and are in non-Darcy flow. In this study, the fracture aperture was fixed, which means that the fracture network and fracture had the same seepage state. In Darcy flow, K does not change with the Reynolds number; in non-Darcy flow, the increase in Re will lead to a decrease in K, which is reflected by the β of the fracture network.

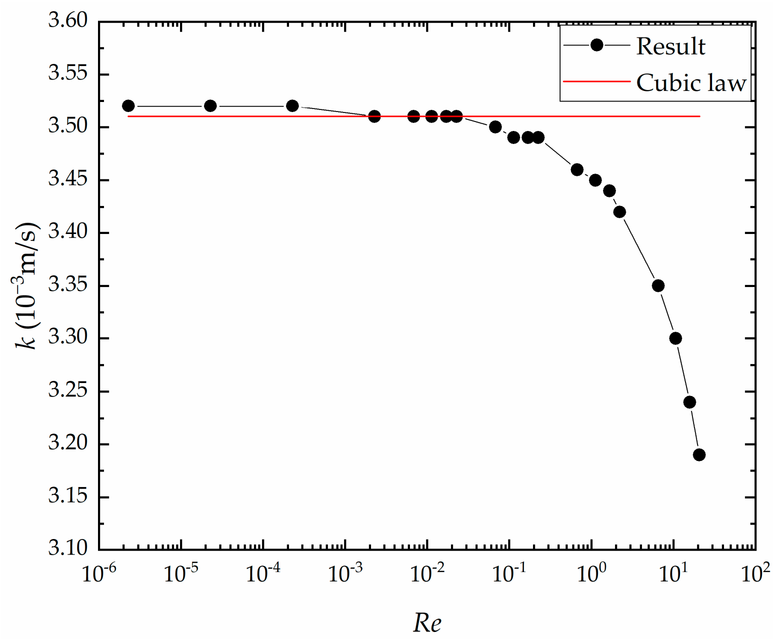

Figure 9. Variation in the hydraulic conductivity of a fracture with different values of *Re*.

In Equations (19) and (20), assuming that the seepage flow is a fixed value, the total hydraulic gradient acting on the fractured rock mass is larger in the non-Darcy flow, which means that the assessment of seepage stability in the Darcy flow will lead to greater potential risks for the fractured rock mass.

5. Discussion

The fractal dimension of the fracture network had a typical size effect. Under the same parameters, it was difficult to generate multiple fractures of small size, which meant that the structure of the fracture network was simple, and the fractal dimension was small, as shown in Figure 10a. With an increase in size, the number of fractures increased rapidly, and the network became complex, indicating that the fractal dimension increased rapidly, as shown in Figure 10b. With a further increase in size, the fracture network became much more complex, and with the increase in the number of fractures, it was difficult to improve the complexity of the network effectively. Although the size was continuously expanded, the growth rate of the fractal dimension continued to decrease and finally reached the critical value.

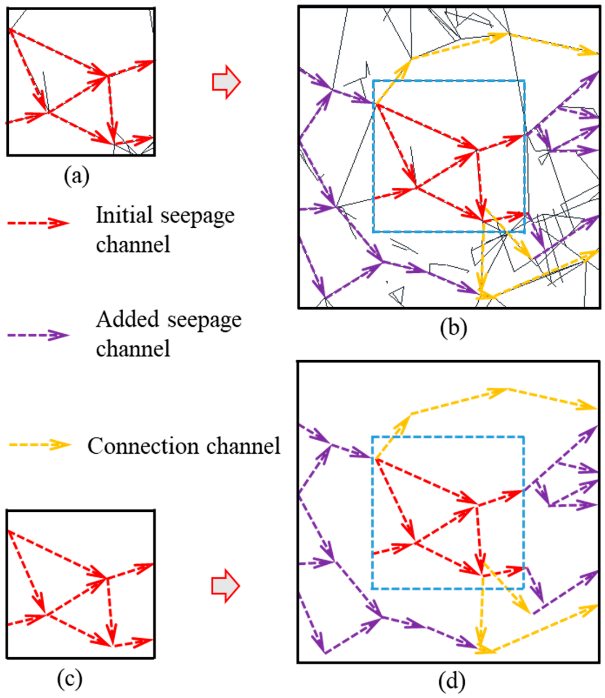

Figure 10. Variation in the fracture network and seepage channel with different sizes. (**a**) Initial fracture network, with a side length of 1 m. (**b**) Expanded fracture network, with a side length of 2 m. (**c**) The seepage channel in the initial fracture network. (**d**) The seepage channel in the expanded fracture network.

When the fracture direction was consistent with the main direction, the fractal dimension of the two-dimensional fracture network tended to be 1, and K and β showed strong anisotropy. When the fractures were distributed in all directions and the structure was very complex, the fractal dimension tended to be 2, and K and β tended to be isotropic.

In Figure 10c,d, with the increase in the analysis area, the fractal dimension and the number of fractures increased rapidly, adding many new seepage channels (purple arrows). In the fracture network with a side length of 2 m, some fractures became unconnected, forming new seepage channels (yellow arrows). When the original fracture was not connected with the new fracture, it blocked the flow of fluid, causing K to decrease and β to increase. When the original fracture was connected with the new fracture, the permeability was maintained, and the fluid flowed through the fracture with little change in K and β. In the main direction of fracture propagation, there were many connected fractures, water flowed more easily, and inertial resistance was relatively small. In other directions, there were few connected fractures, and the inertia resistance of the fluid flow was large, leading to the orthogonality of the seepage ellipse.

Obviously, the new fracture changed the connectivity of the fracture network, causing the permeability to change constantly in all directions, indicating that K and β did not exist. As the growth rate of the fractal dimension slowed, the impact of a new random fracture on the fracture network structure gradually decreased, and K and β gradually became stable in all directions. With the process, K satisfied the existence condition first, and then β began to exist when the fractal dimension tended to be stable. When further increasing the size of the fracture network, K and β will exist and converge with the seepage ellipse.

6. Conclusions

This study proposed a method for simulating high-velocity non-Darcy flow in a fracture network. The fracture network was established according to the geological parameters of Sellafield, Cumbria, England, and 120 internal fracture networks were intercepted according to 10 dimensions and 12 directions. The fractal dimension, equivalent hydraulic conductivity, and equivalent non-Darcy coefficient of the fracture network were calculated. Then, the seepage and fractal characteristics of the fracture network arising from the high-velocity non-Darcy flow were explored. The main conclusions are as follows:

1. The size effect of the fractal dimension of the fracture network was studied, and the change rule of the fractal dimension with size was found. With increases in size, the fractal dimension experienced three processes: rapid increase ($D < 1.559$), slow increase ($1.559 \leq D \leq 1.701$), and tendency to be stable ($D \geq 1.701$).
2. This study proposed a method for simulating non-Darcy flow in a fracture network and explored the influence of the fractal dimension of the fracture network on K and β. In the process of rapid increase, both Darcy and non-Darcy flows in the fracture network were unstable, and K and β did not exist. In the process of slow increase, the Darcy flow in the fracture network reached stability first, and K existed. In the tendency to be stable, the non-Darcy flow finally reached a stable state, and β existed. The effects of random fracture aperture, bias, and roughness were not considered in this study and will be considered gradually in further research.
3. The seepage ellipses of K and β were orthogonal to each other. The main influencing factor was the directivity and connectivity of fracture propagation, which increased the permeability of the fracture network in this direction and reduced the inertial resistance acting on the fluid, indicating that the principal axes of the ellipse were orthogonal to each other.

Author Contributions: Investigation, methodology, writing—original draft preparation, X.Z.; writing—review and editing, project administration, B.Y.; methodology, conceptualization, Y.N.; data curation, C.Y. All authors have read and agreed to the published version of the manuscript.

Funding: This research was funded by the Key Scientific Research Project of Colleges and Universities in Henan Province (22B570002), and the Natural Science Foundation of Henan (222300420281).

Institutional Review Board Statement: Not applicable.

Informed Consent Statement: Not applicable.

Data Availability Statement: The datasets generated during the current study are available from the corresponding author upon reasonable request.

Acknowledgments: The authors would like to thank outstanding young talents training plan by Xuchang University and all the anonymous referees for their constructive comments and suggestions.

Conflicts of Interest: No conflict of interest exists in the submission of this manuscript, and the manuscript was approved by all authors for publication.

References

1. Babadagli, T. Unravelling transport in complex natural fractures with fractal geometry: A comprehensive review and new insights. *J. Hydrol.* **2020**, *587*, 124937. [CrossRef]
2. Hirata, T.; Satoh, T.; Ito, K. Fractal structure of spatial distribution of microfracturing in rock. *Geophys. J. Int.* **1987**, *90*, 369–374. [CrossRef]
3. Miao, T.; Yu, B.; Duan, Y.; Fang, Q. A fractal analysis of permeability for fractured rocks. *Int. J. Heat Mass Transfer.* **2015**, *81*, 75–80. [CrossRef]
4. Saouma, V.E.; Barton, C.C.; Gamaleldin, N.A. Fractal characterization of fracture surfaces in concrete. *Eng. Fract. Mech.* **1990**, *35*, 47–53. [CrossRef]
5. Ren, W.; Xu, J. Fractal characteristics of concrete fragmentation under impact loading. *J. Mater. Civ. Eng.* **2017**, *29*, 04016244. [CrossRef]
6. Wang, L.; Huang, Y.; Zhao, F.; Huo, T.; Chen, E.; Tang, S. Comparison between the influence of finely ground phosphorous slag and fly ash on frost resistance, pore structures and fractal features of hydraulic concrete. *Fractal Fract.* **2022**, *6*, 598. [CrossRef]

7. Min, K.B.; Jing, L.; Stephansson, O. Determining the equivalent permeability tensor for fractured rock masses using a stochastic REV approach: Method and application to the field data from Sellafield, UK. *Hydrogeol. J.* **2004**, *12*, 497–510. [CrossRef]
8. Liang, T.; Liu, X.; Wang, S.; Wang, E.; Li, Q. Study on the fractal characteristics of fracture network evolution induced by mining. *Adv. Civ. Eng.* **2018**, *2018*, 1–13. [CrossRef]
9. Berkowitz, B.; Hadad, A. Fractal and multifractal measures of natural and synthetic fracture networks. *J. Geophys. Res. Solid Earth* **1997**, *102*, 12205–12218. [CrossRef]
10. Tran, N.H.; Rahman, S.S. Development of hot dry rocks by hydraulic stimulation: Natural fracture network simulation. *Theor. Appl. Fract. Mech.* **2007**, *47*, 77–85. [CrossRef]
11. Yang, B.; Liu, Y. Application of fractals to evaluate fractures of rock due to mining. *Fractal Fract.* **2022**, *6*, 96. [CrossRef]
12. Wang, L.; Yu, Z.; Liu, B.; Zhao, F.; Tang, S.; Jin, M. Effects of Fly Ash Dosage on Shrinkage, Crack Resistance and Fractal Characteristics of Face Slab Concrete. *Fractal Fract.* **2022**, *6*, 335. [CrossRef]
13. Carlier, M.A. Causes of the Failure of the Malpasset Dam. In *Foundations for Dams*; ASCE: Reston, VA, USA, 1974; pp. 5–10.
14. Seed, H.B.; Duncan, J.M. The failure of Teton dam. *Eng. Geol.* **1987**, *24*, 173–205. [CrossRef]
15. Liang, D.X.; Jiang, Z.Q.; Zhu, S.Y.; Sun, Q.; Qian, Z.W. Experimental research on water inrush in tunnel construction. *Nat. Hazards* **2016**, *81*, 467–480. [CrossRef]
16. Li, S.; Liu, R.; Zhang, Q.; Zhang, X. Protection against water or mud inrush in tunnels by grouting: A review. *J. Rock Mech. Geotech. Eng.* **2016**, *8*, 753–766. [CrossRef]
17. Wang, L.; Li, G.; Li, X.; Guo, F.; Tang, S.; Lu, X.; Hanif, A. Influence of reactivity and dosage of MgO expansive agent on shrinkage and crack resistance of face slab concrete. *Cem. Conc. Compos.* **2022**, *126*, 104333. [CrossRef]
18. Wang, L.; Zhou, S.; Shi, Y.; Huang, Y.; Zhao, F.; Huo, T.; Tang, S. The influence of fly ash dosages on the permeability, pore structure and fractal features of face slab concrete. *Fractal Fract.* **2022**, *6*, 476. [CrossRef]
19. Perera, M.S.A.; Ranjith, P.G.; Choi, S.K.; Airey, D. Numerical simulation of gas flow through porous sandstone and its experimental validation. *Fuel* **2011**, *90*, 547–554. [CrossRef]
20. MacMinn, C.W.; Szulczewski, M.L.; Juanes, R. CO_2 migration in saline aquifers. Part 1. Capillary trapping under slope and groundwater flow. *J. Fluid Mech.* **2010**, *662*, 329–351. [CrossRef]
21. Louis, C. A study of groundwater flow in jointed rock and its influence on the stability of rock masses, Imperial College. *Rock Mech. Res. Rep.* **1969**, *10*, 1–90.
22. Wilson, C.R.; Witherspoon, P.A. Flow interference effects at fracture intersections. *Water Resour. Res.* **1976**, *12*, 102–104. [CrossRef]
23. Sahimi, M. Flow phenomena in rocks: From continuum models to fractals, percolation, cellular automata, and simulated annealing. *Rev. Mod. Phys.* **1993**, *65*, 1393. [CrossRef]
24. Kosakowski, G.; Berkowitz, B. Flow pattern variability in natural fracture intersections. *Geophys. Res. Lett.* **1999**, *26*, 1765–1768. [CrossRef]
25. Forchheimer, P. Wasserbewegung durch boden. *Z. Ver. Dtsch. Ing.* **1901**, *45*, 1782–1788.
26. Liu, R.; Jiang, Y.; Li, B. Effects of intersection and dead-end of fractures on nonlinear flow and particle transport in rock fracture networks. *Geosci. J.* **2016**, *20*, 415–426. [CrossRef]
27. Zimmerman, R.W.; Al-Yaarubi, A.; Pain, C.C.; Grattoni, C.A. Non-linear regimes of fluid flow in rock fractures. *Int. J. Rock Mech. Min. Sci.* **2004**, *41*, 163–169. [CrossRef]
28. Zhang, Z.; Nemcik, J. Fluid flow regimes and nonlinear flow characteristics in deformable rock fractures. *J. Hydrol.* **2013**, *477*, 139–151. [CrossRef]
29. Long, J.C.; Remer, J.S.; Wilson, C.R.; Witherspoon, P.A. Porous media equivalents for networks of discontinuous fractures. *Water Resour. Res.* **1982**, *18*, 645–658. [CrossRef]
30. Klimczak, C.; Schultz, R.A.; Parashar, R.; Reeves, D.M. Cubic law with aperture-length correlation: Implications for network scale fluid flow. *Hydrogeol. J.* **2010**, *18*, 851–862. [CrossRef]
31. Zhao, Z.; Jing, L.; Neretnieks, I. Evaluation of hydrodynamic dispersion parameters in fractured rocks. *J. Rock Mech. Geotech. Eng.* **2010**, *2*, 243–254. [CrossRef]
32. Zhang, X.; Sanderson, D.J.; Harkness, R.M.; Last, N.C. Evaluation of the 2-D permeability tensor for fractured rock masses. *Int. J. Rock Mech. Min. Sci. Geomech. Abstr. Pergamon* **1996**, *33*, 17–37. [CrossRef]
33. Jafari, A.; Babadagli, T. Estimation of equivalent fracture network permeability using fractal and statistical network properties. *J. Pet. Sci. Eng.* **2012**, *92*, 110–123. [CrossRef]
34. Baghbanan, A.; Jing, L. Hydraulic properties of fractured rock masses with correlated fracture length and aperture. *Int. J. Rock Mech. Min. Sci.* **2007**, *44*, 704–719. [CrossRef]
35. Chen, Y.F.; Zhou, J.Q.; Hu, S.H.; Hu, R.; Zhou, C.B. Evaluation of Forchheimer equation coefficients for non-Darcy flow in deformable rough-walled fractures. *J. Hydrol.* **2015**, *529*, 993–1006. [CrossRef]
36. Wang, Y.; Niu, Y.L.; Feng, Q. Study on the REV Size of Fractured Rock in the Non-Darcy Flow Based on the Dual-Porosity Model. *Geofluids.* **2018**, *2018*, 1–22. [CrossRef]
37. Geertsma, J. Estimating the coefficient of inertial resistance in fluid flow through porous media. *Soc. Pet. Eng. J.* **1974**, *14*, 445–450. [CrossRef]